Chapter 3

Design of Miniaturized BPFs

3.1 Experimental Set-up

This thesis contains four BPF design. The whole process is explained as figure 3-1.

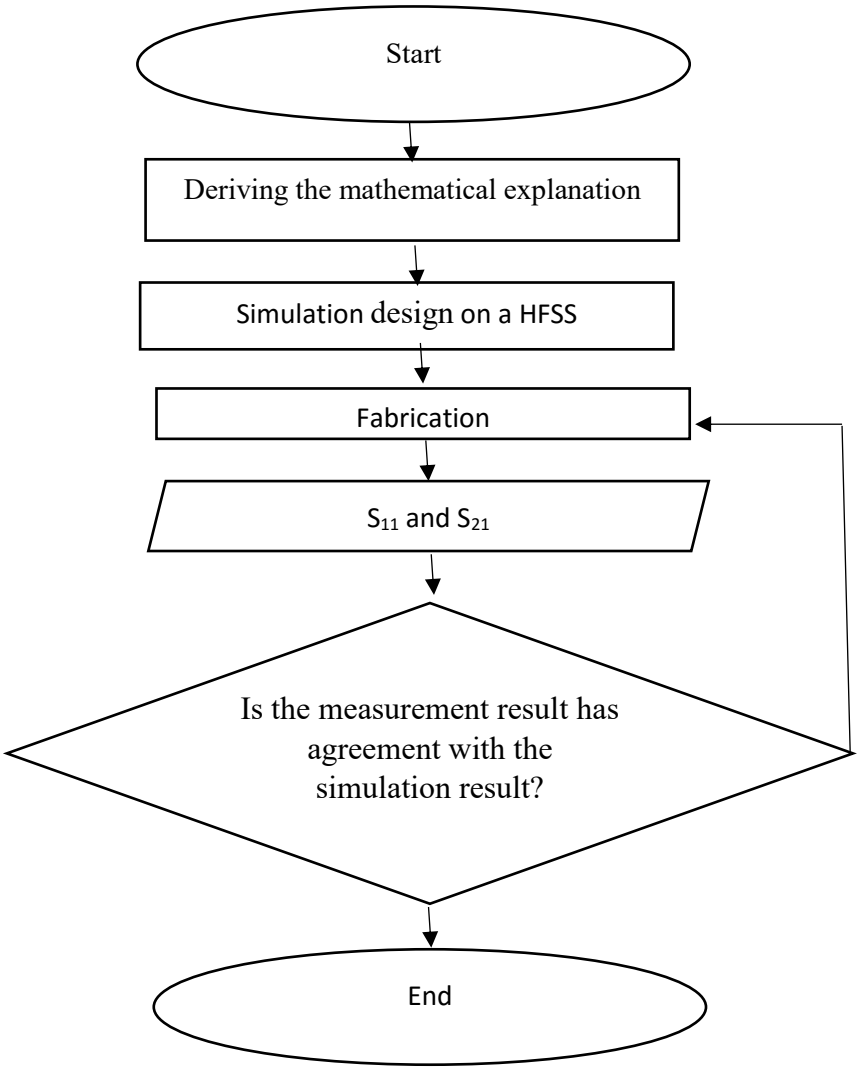

Figure 3.1 Flowchart of the research

The proposed BPFs were fabricated as explained in the next Sub Chapter. The S-parameters of the fabricated filter were measured using a PNA network analyzer. From this measurement, the return losses of the BPFs are obtained from $|S_{11}|$ and the insertion losses are

obtained from $|S_{12}|$. This thesis contains of four BPF designs and will be discussed in the next Sub Chapter.

3.2 Design of One-Band BPF Using FR-4 Substrate

In this study, a miniaturized BPF operates at 3.5 GHz for WIMAX application with an FBW of 7.2% has been proposed. A λ/4 stepped impedance resonator (SIR) with two additional via holes has been adopted to obtain a compact size and a pair of TZs. This study provides a simple and effective method to design a low loss, wide rejection band and compact BPF with a tunable TZ without complex topology and fabrication process.

3.2.1 Design Procedure

Figure 3.2 shows the geometry of the proposed miniaturized BPF. In this figure, a pair of λ/4 SIR resonators with two via holes have been implemented using a FR-4 substrate with the thickness of 0.8 mm. These resonators are connected to the ground plane by means of via hole.

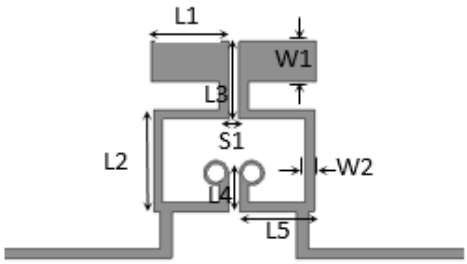

Figure 3.2 Structure of BPF (L1=2.5, L2=3.3, L3=2.5, L4=1.3, L5=2.5, W1=1.3, W2=0.3, S1=0.3. All are in mm)

The external quality factor (Q_e) and coupling coefficients (k) are the two most important parameters for a coupled resonator BPF design. To obtain Q_e, the proper tapped feed position (P_t) needs to be tuned carefully. The coupling coefficient can be obtained as a function of the gap spacing (S) between the two resonators as shown in figure 3-3. The coupling coefficient can be written as

$$K_{i,i+1} = \pm\frac{f_2^2 - f_1^2}{f_2^2 + f_1^2} \quad \text{.....(3-1)}$$

where f_1 and f_2 are the two dominants resonant frequencies. Moreover, the external quality factor of this BPF design can be calculated as

$$Q_e = \frac{\omega_0 \tau_r(\omega_0)}{4}[1 - y_{in}^2(\omega_0] \quad \text{.....(3-2)}$$

where ω_0 is the resonant angular frequency, y_{in} and τ_r can be obtained from the reflection coefficient and the derivative of its phase with respect to angular frequency, respectively.

The coefficient *k* can be determined as a function of *S* by using an electromagnetic (EM) simulator and the result is shown in figure 3-3. To determine *S* and P_t for an nth-order BPF design, one can use the relations of the $k_{i,i+1}$ and Q_e with the filter prototype elements. These relations are given as

$$k_{i,1+1} = \frac{\Delta}{\sqrt{g_i g_{i+1}}} \quad \text{.....(3-3)}$$

$$Q_e = \frac{g_1}{\Delta} = \frac{g_n g_{n+1}}{\Delta} \quad \text{.....(3-4)}$$

where Δ is the fractional bandwidth and g_i is the *ith* prototype element value of a second-order 0.2 dB equal-ripple Chebyshev BPF. The prototype element values used are g_1 = 1.403, g_2 = 0.707, and g_3 = 1.984. The coupling coefficient ($k_{1,2}$) and the quality factor (Q_e) estimated by calculation are 0.072 and 19.39, respectively. It can be found from Figure 3-3 and figure 3-4 that the $k_{1,2}$ and Q_e values correspond to $S_{c1,2}$ = 300 μm and P_t = 2.2 mm.

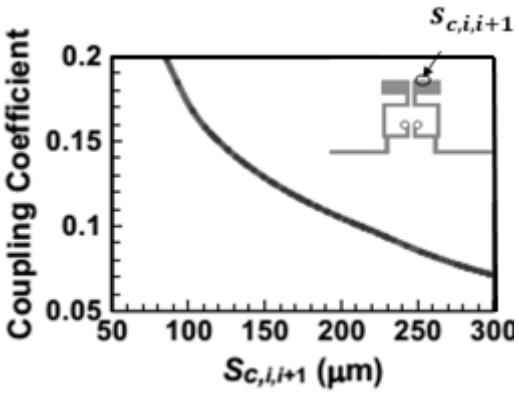

Figure 3.3 Coupling coefficient versus the spacing between two coupled resonators

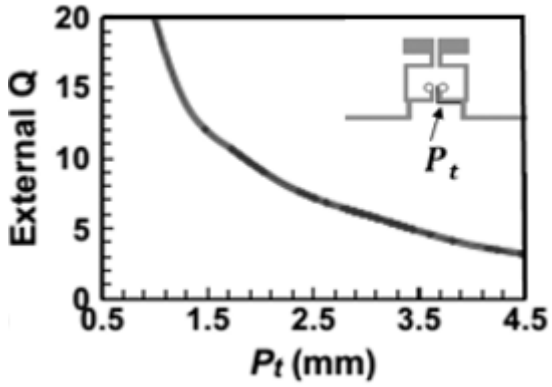

Figure 3.4 External quality factor versus the tapped position of the input/output port for a single resonator.

3.2.2 Result and Approach for Tunable TZs

Figure 3-5 shows the comparison of *S*-parameters between simulation and measurement for the designed BPF. The return loss is approximately larger than 18 dB and the insertion loss is about 2 dB in the passband. The simulation results agree well with the measurements. Two TZs are located at 2.7 and 5.2 GHz, respectively. As the photograph of Figure 3-6 shows, the overall size of the designed BPF is 4.2 mm × 5.2 mm.

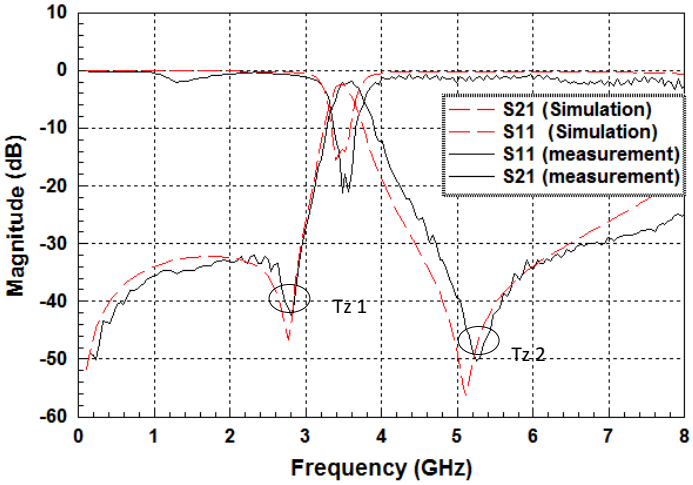

Figure 3.5 The simulation and measurement result

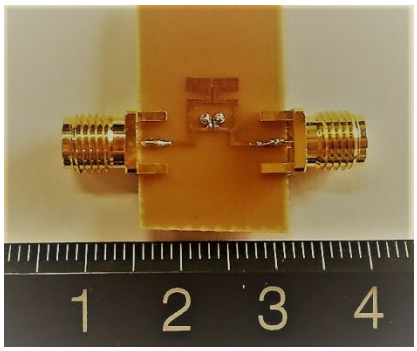

Figure 3.6 Photograph of fabricated BPF

This work also develops a novel approach to tune the TZs. There are three ways to tune the TZs in this proposed BPF design. The TZs can be tuned by adjusting the parameter *S*, as shown in figure 3.7. The TZs of the BPF can be controlled by adjusting the parameters *S*, W_1 (width of the top resonator) and L_3 (length of the resonator's neck), as depicted in figure 3-2.

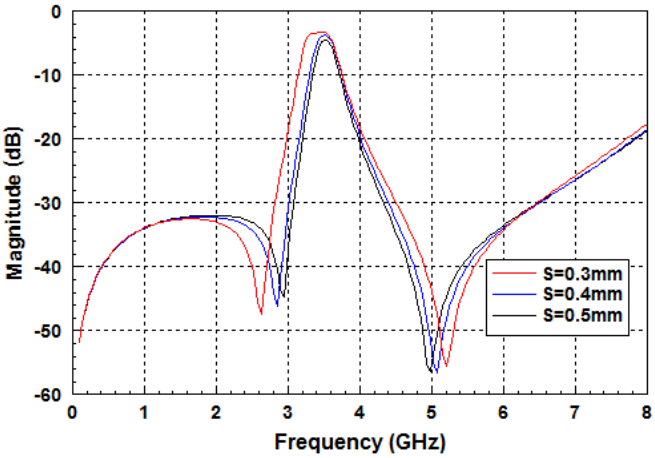

Figure 3.7 The TZ frequency shift due to the adjustment of *S*.

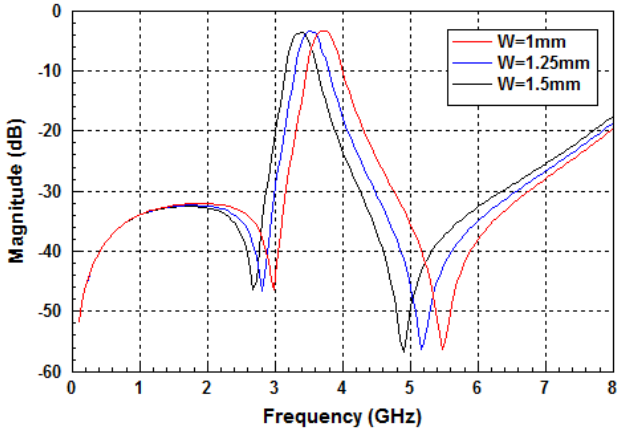

Figure 3.8 The TZ frequency shift due to the adjustment of W_1.

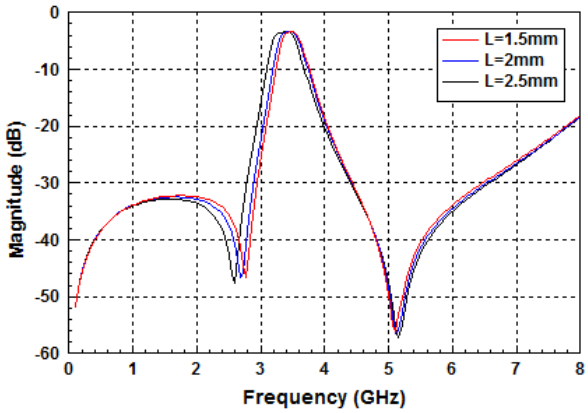

Figure 3.9. The TZ frequency shift due to the adjustment of L_3.

For the gap spacing effect, as *S* gets larger, the TZs move closer to the passband, which makes the passband narrower, as shown in *Figure 3.7*. This is because the coupling

coefficient becomes weaker when S is larger. Moreover, these TZs cause a higher roll-off rate for passband-to-stopband transition. *Figure 3.8* shows that the TZs shift to the lower frequencies as the width of the top resonator gets wider. If we want to tune the first TZ only, we can adjust the length of L_3. As seen in *Figure 3.9*, the first TZ shifts to lower frequencies as L_3 decreases.

3.3 Miniaturized BPF Using Additional Ring Slot

In this study, a new concept of tunable TZs for one-band BPF is demonstrated. A quarter wavelength stepped impedance resonator (SIR) has been adopted to miniaturize the occupied filter area. A novel approach is also proposed to tune the TZs. This approach involves a ring slot in the bottom ground plane without adding resonators or increasing component size. By adjusting the diameter of the ring slots, the TZs can be controlled effectively.

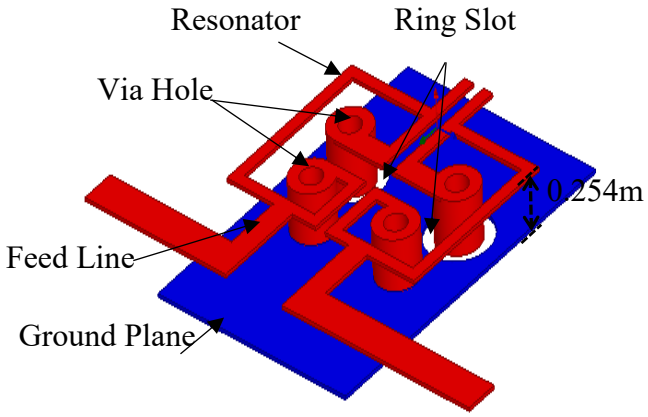

Figure 3.10 3-D look of the filter topology

3.3.1 Filter Design Procedure

A second-order one-band BPF has been simulated and implemented in a RT/Duroid 6010 substrate with dielectric constant of 10.2, as shown in Figure 3-10 The filter occupied 4 mm × 3.8 mm in area. It is constructed by an *LC* resonator with 4 via holes. Two via holes contact the ground plane and the rest of them are separated by the ring slots. This study demonstrated that a pair of TZs can be obtained by replying on the gap between the resonators (electrical coupling) and the via holes shorted to the ground plane (magnetic coupling). The additional via holes with the slots are used to tune the TZ frequencies efficiently.

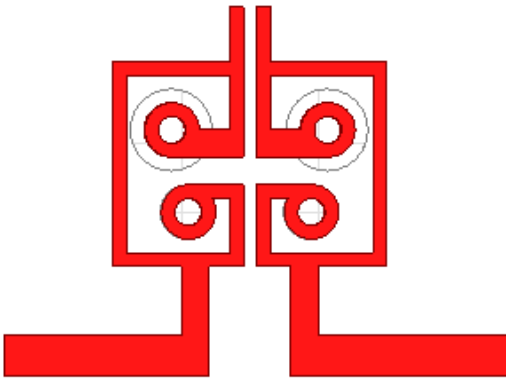

a)

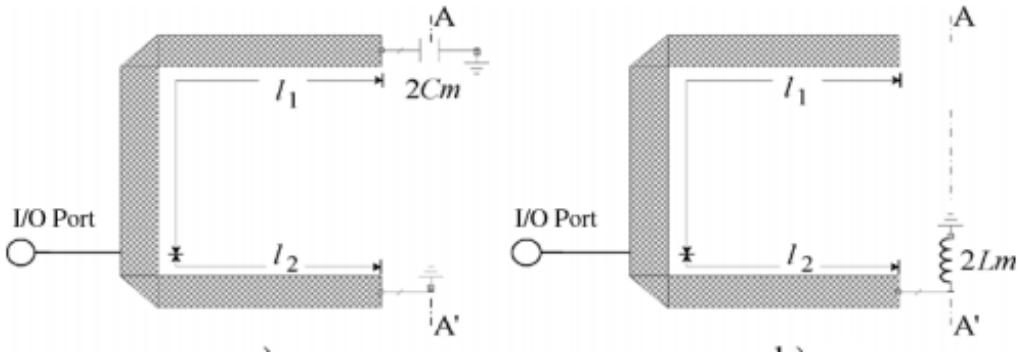

b) c)

Figure 3.11 The equivalent odd- and even- mode configuration (a) Top view layout. (b) the even mode. (c) the odd mode.

The two most important parameters in this BPF design are the coupling coefficient and external quality factor. Based on the even and odd mode analysis, the following parameters are given as

$$L_{odd} = L - L_m \quad \text{.....(3-5)}$$

$$L_{even} = L + L_m + L_{slot} \quad \text{.....(3-6)}$$

$$C_{odd} = C + C_m + C_{slot} \quad \text{.....(3-7)}$$

$$C_{even} = C - C_m \quad \text{.....(3-8)}$$

The resonant angular frequencies of even and odd modes can be expressed in terms of the above parameters as

$$\omega_{odd} = \frac{1}{\sqrt{L_{odd}C_{odd}}} \quad \text{.....(3-9)}$$

$$\omega_{even} = \frac{1}{\sqrt{L_{even}C_{even}}} \quad \text{.....(3-10)}$$

A natural resonant angular frequency is defined as

$$\omega_o = \frac{1}{\sqrt{LC}} \quad \text{.....(3-11)}$$

From [7], we further obtain

$$\left(\frac{\omega_o}{\omega_{odd}}\right)^2 = \frac{1+k_e}{1+k_m} \quad \text{.....(3-12)}$$

$$\left(\frac{\omega_o}{\omega_{even}}\right)^2 = \frac{1-k_e}{1-k_m} \quad \text{.....(3-13)}$$

where k_m and k_e are derived as

$$k_m = \frac{2\omega_{odd}^2\omega_{even}^2 - \omega_o^2\left(\omega_{even}^2 + \omega_{odd}^2\right)}{\omega_o^2\left(\omega_{even}^2 - \omega_{odd}^2\right)} \quad \text{.....(3-14)}$$

$$k_e = \frac{2\omega_o^2 - \left(\omega_{even}^2 + \omega_{odd}^2\right)}{\left(\omega_{odd}^2 - \omega_{even}^2\right)} \quad \text{.....(3-15)}$$

In (3-14) and (3-15), k_m is the magnetic coupling coefficient and k_e is the electric coupling coefficient. The total coupling coefficient is $k = k_m - k_e$. Notably, the magnetic and electric coupling mainly arises from the two short-circuited via holes and the two gap-coupled SIR, respectively. Therefore, the spacing between the two short-circuited via holes and the gap width between the two resonators can be adjusted to obtain the desired coupling coefficient *k*. Moreover, as 3-16 shows, the external quality factor Q_e can be derived in terms of the input admittance y_{in} and the group delay τ_T that are obtained from the reflection coefficient and the derivative of its phase with respect to angular frequency, respectively.

$$Q_e = \frac{\omega_o \tau(\omega_o)}{4}\left(1 - y_{in}^2(\omega_o)\right) \quad \text{.....(3-16)}$$

The values of *k* and Q_e are calculated according to

$$k_{i,i+1} = \frac{FBW}{\sqrt{g_i g_{i+1}}} \quad \text{.....(3-17)}$$

$$Q_e = \frac{g_1}{FBW} = \frac{g_n g_{n+1}}{FBW} \quad \text{.....(3-18)}$$

where FBW is the fractional bandwidth and g_i is the i_{th} prototype element value of a second-order 0.2 dB equal-ripple Chebyshev BPF. In this design, $g_1 = 1.038$, $g_2 = 0.675$, and $g_3 = 1.539$. Generally speaking, the coupling coefficient determines the fractional bandwidth of the passbands while the external quality factor determines the tapped position of feed ports.

3.3.2 Result and Analysis

A single band second-order 0.2 dB Chebyshev BPF is designed with the FBW of 7% and the center frequency of 5.8 GHz. The prototype element values used are $g_1 = 1.403$, $g_2 = 0.707$, and $g_3 = 1.984$. The coupling coefficient (k) and the quality factor (Q_e) estimated by calculation are 0.072 and 19.39, respectively.

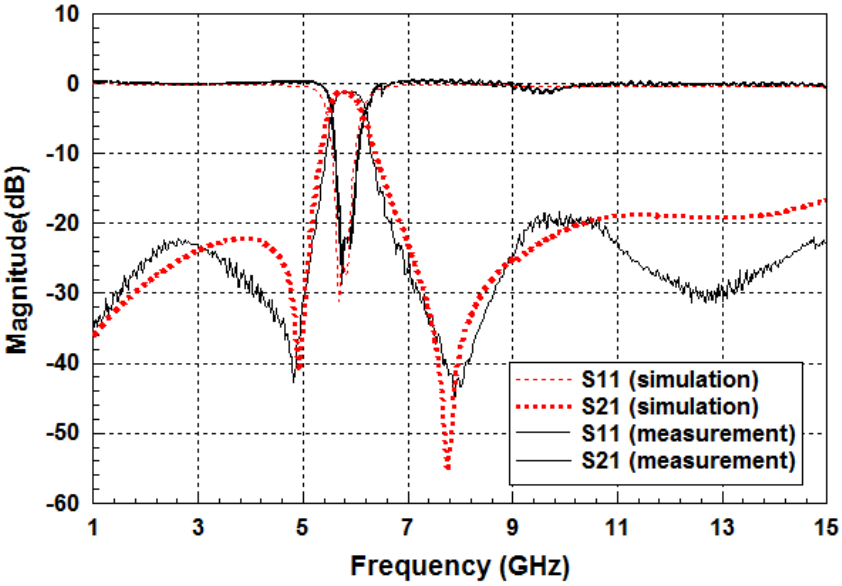

Figure 3.12 The simulation and measurement results

Figure 3.12 compares the simulation and measurement results. The comparison shows good agreement. The measurement results reveal that the insertion loss is less than 1.1 dB and the return loss is approximately 23 dB. The BPF design produces two TZs at 4.9 and 7.7 GHz on both side of the passband. These two TZs can be controlled by the magnetic and electric coupling coefficients as shown in Eqn. 3-12.

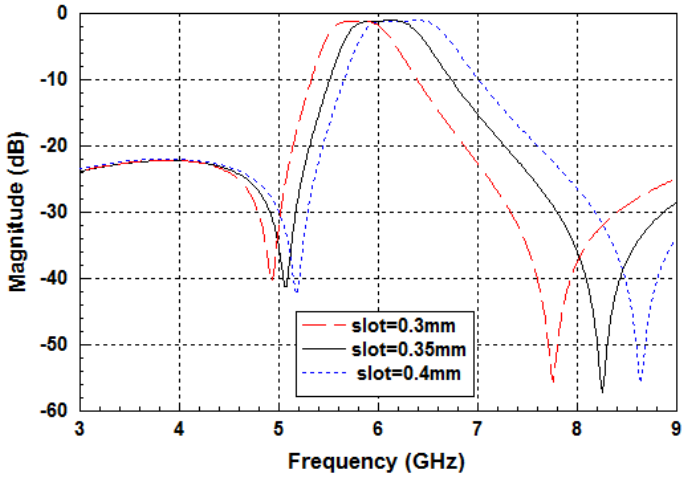

Figure 3.13 Comparison of slot diameter effect to TZ

This study also proposes a simple approach for controlling the TZ frequencies. The proposed approach puts an additional via hole and a ring slot in the ground plane to increase both L_m and C_m. When the C_m and L_m are increased, the operating center frequency goes lower when the coupling coefficients are kept fixed. By adjusting the additional via hole and the ring slot, the TZs can be controlled efficiently, as shown in Figure 3-13. From this figure, as the diameter of ring slots increases, the TZs shift to higher frequencies. This is because the parasitic capacitance of the ring slots C_{slot} decreases as the diameter increases.

3.4 Design of Tri-band BPF

This study aims at developing new concept of multiband BPF using stacked stepped impedance resonator (SSIR) with controllable TZs. The proposed filter is designed at 2.4/5.8/10.6 GHz for WLAN (2.4/5.8 GHz) and 5G (10.6 GHz) systems. A novel approach to tune the TZs is also proposed. This approach involves some ring slots in the bottom ground plane. By adjusting the diameter of the ring slots, the TZs can be controlled efficiently without adding resonators or increasing the component size.

3.4.1 Design Procedure

As shown in Figure 3-13, a three-layer SSIR has been designed on a 0.568 mm thick three-layer RT/Duroid 6010 substrate with dielectric constant of 10.2. It occupies an area of 2.8 mm × 1.2 mm. It uses three via holes. One via hole is short-circuited by connecting it to the ground plane; another via hole is open-circuited by isolating it from

the ground plane with a ring slot, and the other via hole serves as an interconnect between the first and second metal layers. This forms a quarter-wave short-circuited SSIR on which the proposed BPF is based.

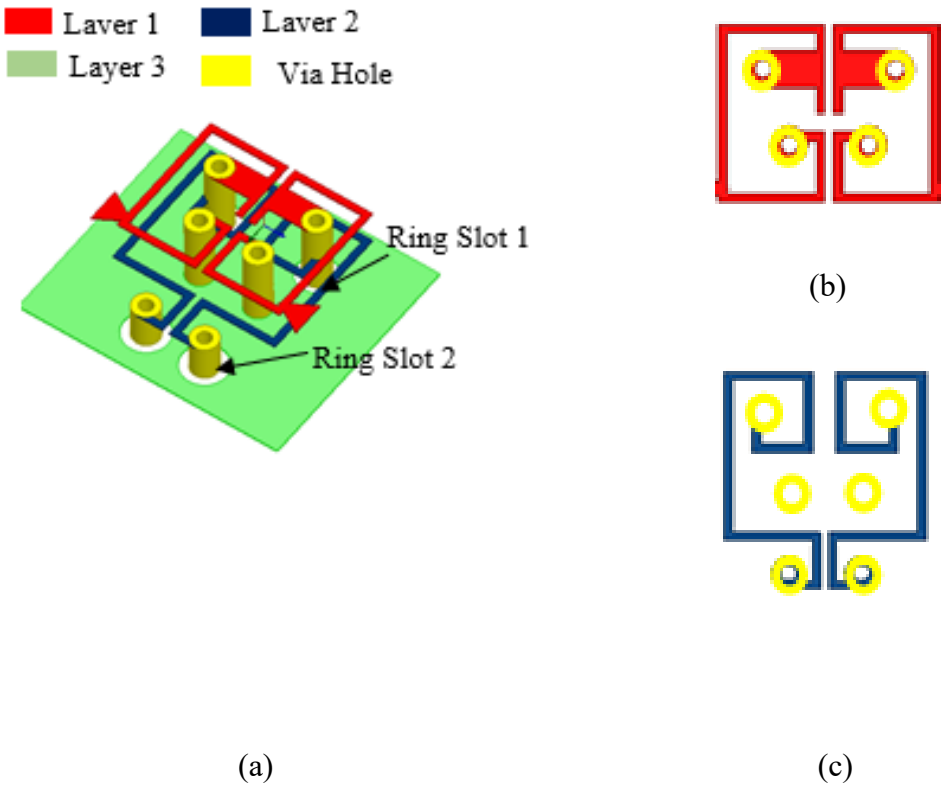

Figure 3.13. (a) Proposed Tri-band BPF design (b) Layer 1 metal pattern (c) Layer 2 metal pattern

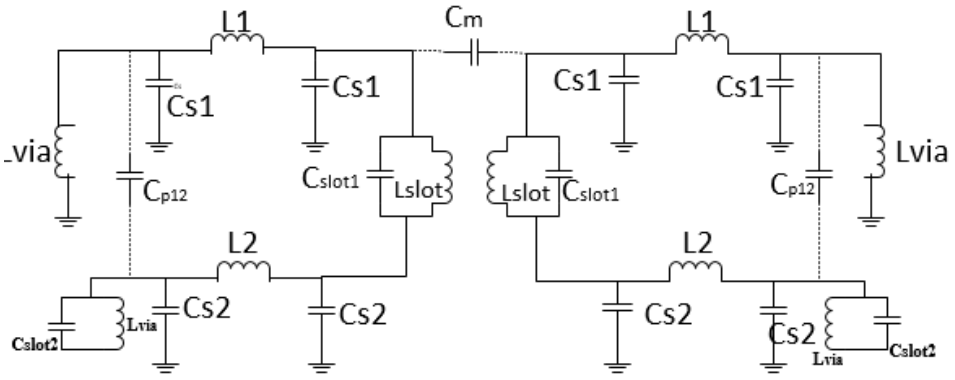

Figure 3.14 The equivalent circuit of the proposed BPF using coupled SSIRs.

Figure 3.14 displays the equivalent circuit of the coupled SSIR BPF design without considering the resistive loss, where C_{si} denotes the metal-to-ground capacitance

of the resonator, C_{p12} and M_{12} represent the capacitance and mutual inductance between L_1 and L_2, respectively. By assuming $C_{s1}<<C_{s2}$ and $M_{12}<<(L_1+3L_{via})$, the first two resonant angular frequencies of the SSIR can be obtained as

$$\omega_1 = \sqrt{\frac{1}{2(C_{s2}+C_{slot1}+C_{slot2})L_{1T}}} \quad \text{.....(3-19)}$$

$$\omega_2 = \sqrt{\frac{1}{C_{s2}+C_{slot1}}\left(\frac{1}{2L_{1T}}+\frac{2}{L_3-M_{12}}\right)} \quad \text{.....(3-20)}$$

where

$$L_{1T} = L_1 + 3L_{via} \quad \text{.....(3-21)}$$

and the third resonant frequency can be obtained by using the following relation:

$$\frac{\omega_3}{\omega_1} = \frac{\pi}{\tan^{-1}\sqrt{R}} - 1 \quad \text{.....(3-22)}$$

where R denotes the impedance ratio Z_2/Z_1 on the second layer. The above results indicate that the third resonant frequency ω_3 can be obtained by designing the impedance ratio R with a predetermined ω_1, as shown in Figure 3-15. Notably, the L_1 and L_2 in Figure 3-14 are wound clockwise and counterclockwise, respectively, resulting in a negative mutual inductance ($M_{12}<0$). This negative mutual inductance reduces the need of a high-impedance microstrip line.

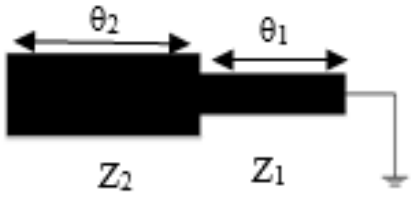

Figure 3.15 Two-section SIR configurations.

To demonstrate the feasibility of the proposed design concept, this work designs a second-order 0.2-dB equal-ripple Chebyshev. The values of k and Q_e are calculated according to

$$k_{i,i+1} = \frac{FBW}{\sqrt{g_i g_{i+1}}} \quad \text{.....(3-23)}$$

$$Q_e = \frac{g_1}{FBW} = \frac{g_n g_{n+1}}{FBW} \quad \text{.....(3-24)}$$

where FBW is the fractional bandwidth and g_i is the i_{th} prototype element value of a second-order 0.2 dB equal-ripple Chebyshev BPF. In this design, g_1 = 1.038, g_2 = 0.675, and g_3 = 1.539. Generally speaking, the coupling coefficient determines the fractional bandwidth of the passbands while the external quality factor determines the tapped position of feed ports.

3.4.3. Analysis and results of a Tri-band BPF

A tri-band BPF with the passband center frequncies of 2.4, 5.8 and 10.6 GHz and the passband fractional bandwidth of 8.9, 13.5 and 4 % respectively was designed based on the coupling of a pair of SSIRs with the specific via holes and ring slots. This tri-band BPF was implemented in a three-layer RT/Duroid 6010 substrate.

The coupling coefficient (k) and the external quality factors (Q_e) can be obtained by adjusting the gap spacing between the SSIRs and the tapped position of the feed ports. The coupling coefficient (k) and external quality factors (Q_e) are estimated as Q_{e1}= 15.2 and k_1=0.091 for the first passband, Q_{e2}= 10.05 and k_2=0.15 for the second passband and Q_{e3}= 33.93 and k_3=0.04 for the third passband.

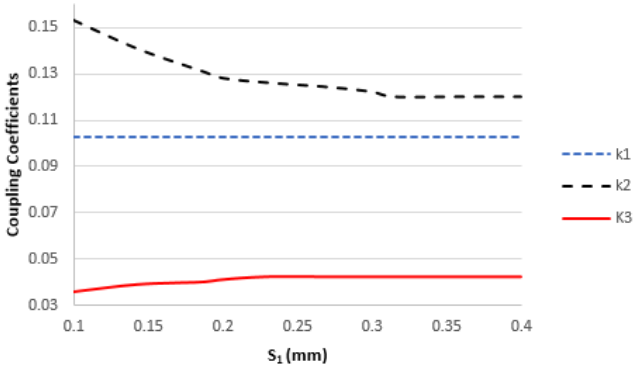

(a)

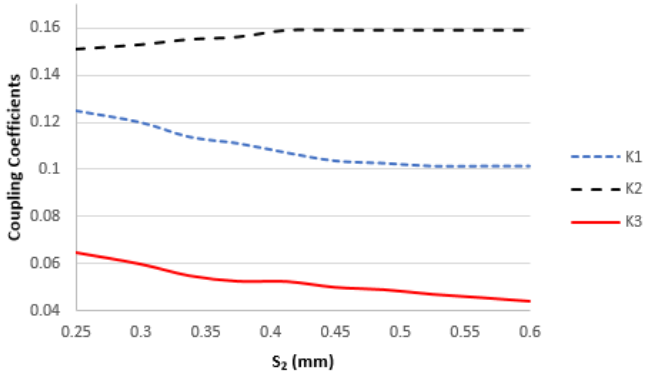

(b)

Figure 3.16 Spacing gap resonator on each layer versus coupling coefficients. (a) Metal layer1 (b) Metal layer 2

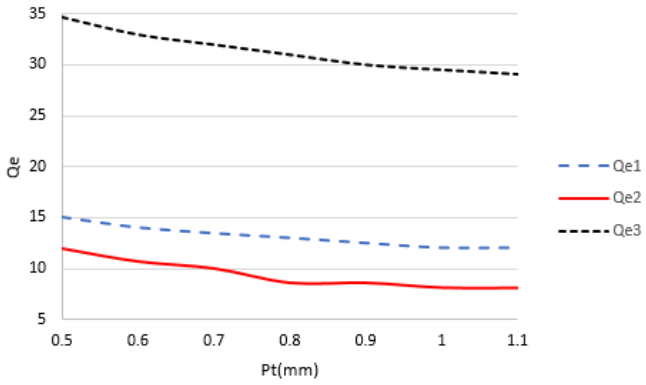

Figure 3.17 External quality factors versus the tapped feed position

Figure 3.16 (a) and (b) shows the coupling coefficients with respect to gap spacing on the first layer and the third layer, respectively. According to Figure 3.16 (a), when S_1 increases, the second passband coupling coefficient is obviously decreased without changing the coupling coefficients of the first and third passband. This is because the resonator gap spacing dominates the electric coupling of the design. It has been further observed from HFSS simulation that the second coupling coefficient k_2 is strongly affected by the resonator gap in the first layer. Meanwhile, the first and third coupling coefficients, k_1 and k_3, are mostly affected by the resonator gap in the second layer. The values of Q_e are closely related to the position of the feedline P_t. As P_t increases, the values of Q_e of all passbands are decreased. Moreover, the bandwidth also alters the value

of Q_e. It has been simulated from HFSS simulation that Q_e decreases as the bandwidth increases.

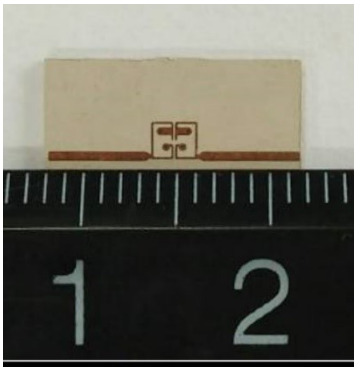

Figure 3.18 photograph of proposed design

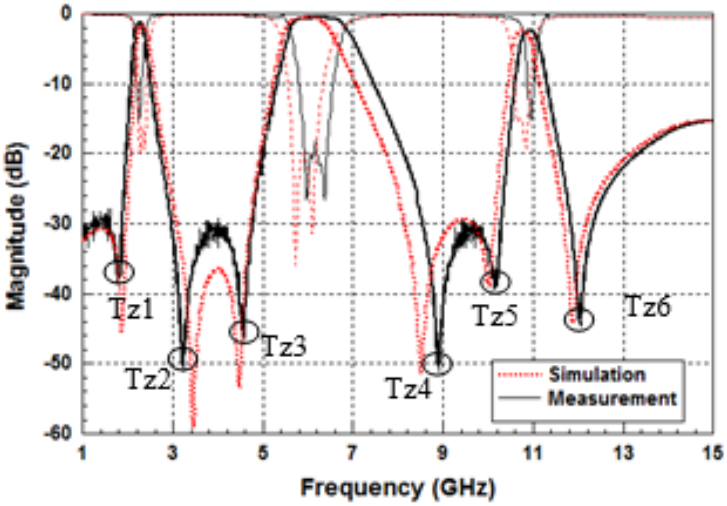

Figure 3.19 Simulated and measured frequency responses of the designed quadband BPF

Figure 3.19 compares the magnitudes of S_{11} and S_{21} between simulation and measurement, indicating a good agreement over a frequency range up to 15 GHz. The measured return losses in all passband are less than 12 dB. The insertion losses are less than 1.66, 0.7, and 2.4 dB in the first, second and third passband, respectively.

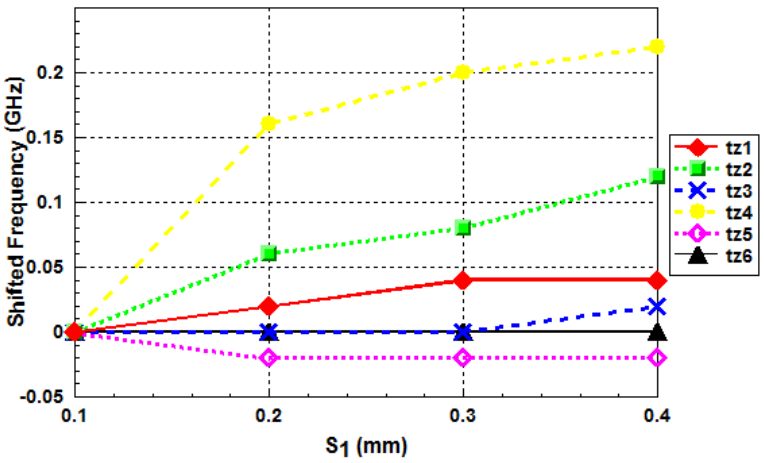

Figure 3.20 TZ frequencies versus the resonator gap spacing in first layer

The spacing gap between the resonators affects the electric coupling. Therefore, a change of the spacing gap can shift the TZ frequencies, as depicted in Figure 3.20 and Figure 3.21. According to the Figure 3.20, when the spacing gap in the first layer increases, the second and fourth TZs are obviously pushed to higher frequencies while the first TZ increases slightly in frequency and the fifth TZ shifts to a lower frequency. Meanwhile, the other TZs remains the same. It means that the spacing gap in the first layer affects much on the second passband. Figure 3.21 shows the influences of spacing gap in the second layer on the TZs. According to the Figure 3.21, when the spacing gap in the second layer increases, the sixth TZ is dramatically pushed to a higher frequency while the fifth TZ shifts to a lower frequency. The other TZs almost remains the same frequency.

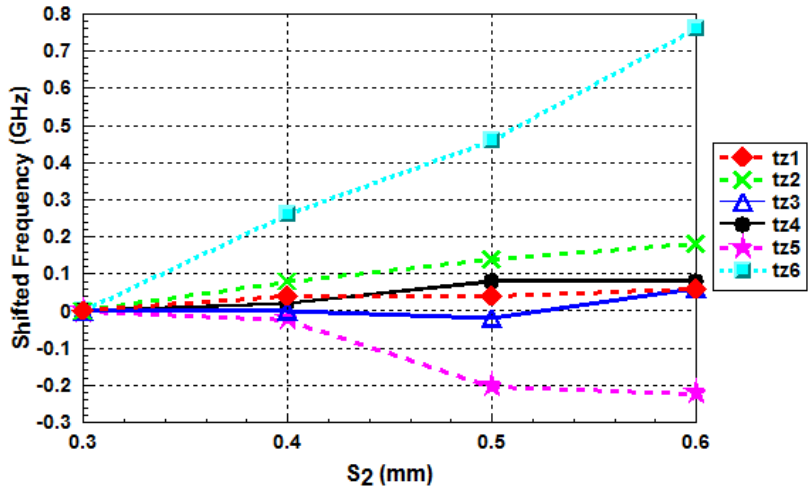

Figure 3.21 TZ frequencies versus the resonator gap spacing in second layer

This work also proposes a simple approach for controlling the TZ frequencies. The proposed approach puts an additional via hole with a ring slot in the ground plane to increase both inductance and capacitance. When the inductance and capacitance are increased, the operating center frequencies shift to lower frequencies while the coupling coefficients are unchanged. Therefore, the TZ frequencies can be tuned efficiently by changing the via hole and ring slot.

The ring slots in the resonator's ground plane affect the electric coupling and therefore a change of the gap spacing can shift the TZ frequencies, as depicted in Figure 3.22 and Figure 3.23. According to the Figure 3.22, an increase in the diameter of ring slot 1 dramatically pushes the fourth TZ to a higher frequency but moves the fifth TZ to a lower frequency. Meanwhile, the other TZs remain the same frequency. Since the TZs around the second and third passbands are pushed away from the passbands, the roll-off rates in these passband reduce. Figure 3.23 shows the influences of the ring slot 2 on the TZs. It reveals that as the diameter of the ring slot 2 increases, the fourth and sixth TZs move to higher frequencies.

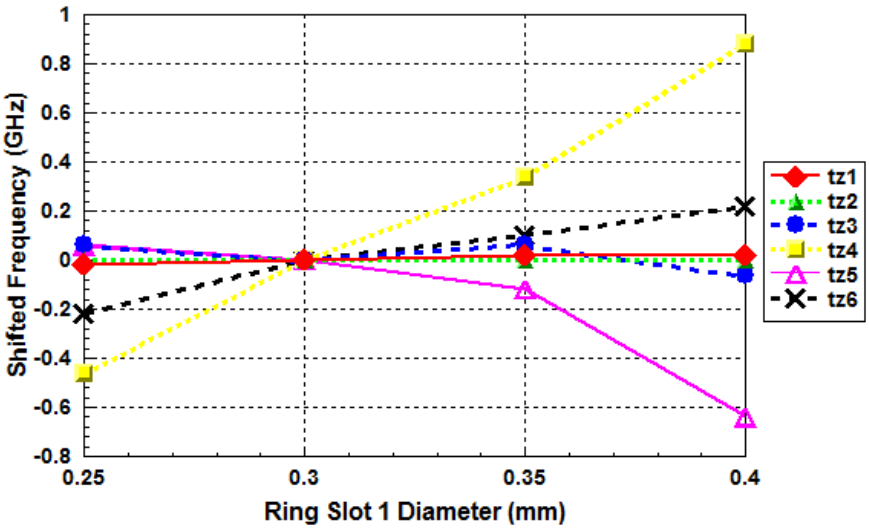

Figure 3.22 TZ frequencies versus the diameter of ring slots

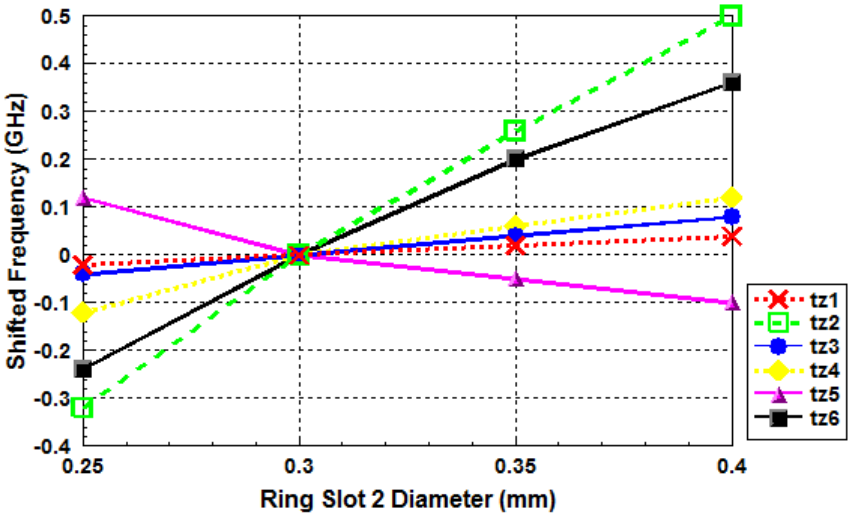

Figure 3.23 TZ frequencies versus the diameter of ring slots

Although the ring SIR has good ability to shift the higher-order resonant mode to form another passband, it generally requires a large occupied area. This work uses the multilayer SIR to reduce the occupied area, resulting a BPF with compact size, good stopband rejection and high selectivity. Each stopband has at least two TZs to improve the rejection.

Table-1 Performance comparison of triband BPFs

Reference Number	Substrate parameter	Passband center frequency (GHz)	3-dB FBW (%)	Passband insertion loss (dB)	Size (mm) & (λg)
[38]	ε_r = 3.38 h = 0.508	2.5/3.6/5.1	4.0%/3.8%/ 6.0%	2.9/2.7/2.3	32.5 x 29.1 (0.5x0.45)
[39]	ε_r = 4.5, h = 0.8	1.57/3.5/5.8	5.0%/14%/3 .2%	1.1/1.4/1.6 6	11.2 x 9.3 (0.12x0.1)
[40]	ε_r = 2.65, h = 1.0	2.4/3.5/5.25	8.6%/7.8%/ 4.9%	1.57/1.66/ 1.5	36.8 x 39.2(0.48x0.51)
[41]	ε_r = 2.2, h = 0.787	1.37/2.43/3.53	4.4%/5.9%/ 2.7%	1.7/1.8/2.5	39.9 x 20.4 (0.27x0.14)
Proposed design	ε_r = 10.2, h = 0.568	2.4/5.8/10.6	8.9%/13.5% /4%	1.66/0.7/2. 4	2.8 x 2.5 (0.071x0.063)

Table-1 compares the performance between the proposed BPF and the previous works. It can be seen that the proposed BPF has a smaller size because its multilayer structure can reduce size significantly. Moreover, the proposed BPF has a lower insertion loss.

3.5 Design of Quadband BPF

A second-order quadband BPF has been simulated and fabricated in an RT/Duroid 6010 substrate with dielectric constant of 10.2, as shown in Figure 3-24. This filter occupies an area of 2.6 mm × 2.5 mm. It consists of an SIR with 4 via holes. Two via holes connect to the ground plane and the rest of them are isolated from the ground plane by the ring slots. Two dual-bands are created by two pairs of stacked dual-mode resonators.

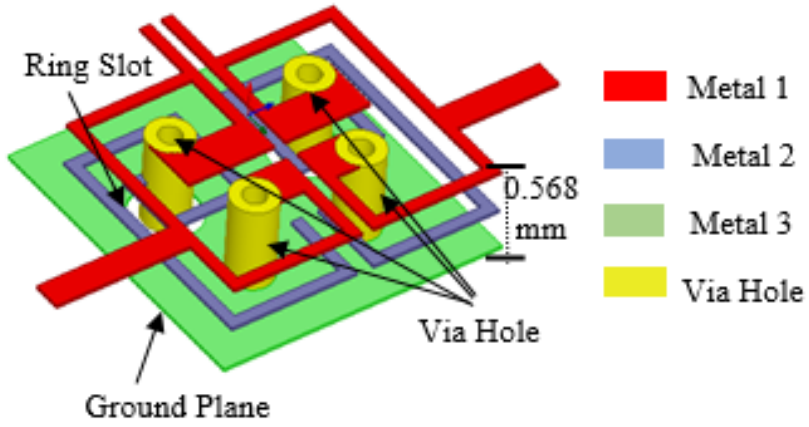

Figure 3.24 3D configuration of the proposed quad-band BPF.

3.5.1 Design Procedure

As shown in Figure 3-25, a second-order quad-band BPF has been designed on a 0.568 mm thick three-layer RT/Duroid 6010 substrate with dielectric constant of 10.2. It occupies an area of 2.6 mm × 2.5 mm. It can be viewed to consist of two symmetric SSIRs with four via holes. Two via holes connect to the ground plane for short circuit purpose. The other two via holes serve as interconnects between the first and second metal layers. This forms a coupled quarter-wave short-circuited SSIRs on which the proposed BPF is based.

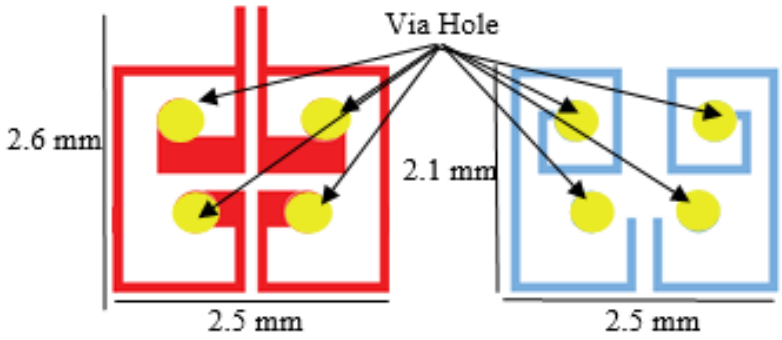

(a)

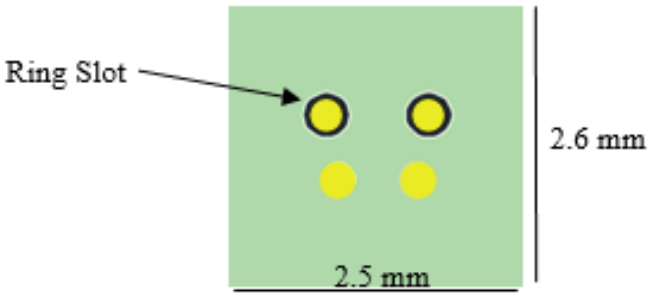

(b)

Figure 3.25 BPF's metallic patterns. (a) First layer. (b) Second layer. (c) Third layer (ground plane).

The advantages of the designed BPF include small size and ease of adjusting coupling coefficients between two SSIRs. A simplified equivalent circuit of the designed BPF is shown in Figure 3-26 where L and C are the self-inductance and self-capacitance of the SSIR, and L_m and C_m are the magnetic and electric coupling coefficients between two SSIRs.

The two most important parameters in this BPF design are the coupling coefficient and external quality factor. Based on the even and odd mode analysis as described in (3-5) – (3-15), the coupling coefficient is obtained as $k = k_m - k_e$, where k_m is the magnetic coupling coefficient and k_e is the electric coupling coefficient. Notably, the magnetic and electric coupling mainly arises from the two short-circuited via holes and the two gap-coupled SSIRs, respectively. Therefore, the spacing between the two short-circuited via holes and the gap width between the two SSIRs can be adjusted to obtain the desired coupling coefficient k.

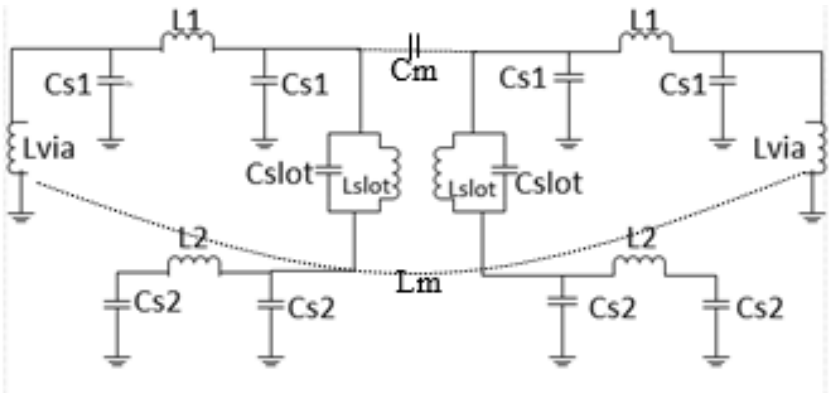

Figure 3.26 The equivalent circuit of the proposed BPF.

As equation (3-25) shows, the external quality factor Q_e can be derived in terms of the input admittance y_{in} and the group delay τ_Γ that are obtained from the reflection coefficient and the derivative of its phase with respect to angular frequency, respectively.

$$Q_e = \frac{\omega_0 \tau(\omega_0)}{4}\left(1 - y_{in}^2(\omega_0)\right) \quad \text{.....(3-25)}$$

The values of k and Q_e are calculated according to

$$k_{i,i+1} = \frac{FBW}{\sqrt{g_i g_{i+1}}} \quad \text{.....(3-26)}$$

$$Q_e = \frac{g_1}{FBW} = \frac{g_n g_{n+1}}{FBW} \quad \text{.....(3-27)}$$

where FBW is the fractional bandwidth and g_i is the i_{th} prototype element value of a second-order 0.2 dB equal-ripple Chebyshev BPF. In this design, $g_1 = 1.038$, $g_2 = 0.675$, and $g_3 = 1.539$. Generally speaking, the coupling coefficient determines the fractional bandwidth of the passbands while the external quality factor determines the tapped position of feed ports.

3.5.3 Result And Analysis

A three-layer quad-band BPF has been implemented with the passband center frequencies of 2.4 GHz, 5.8 GHz, 11.6 GHz and 19 GHz and the fractional bandwidths of 4.1%, 12.5%, 6.29% and 7%, respectively. The desired coupling coefficients and external quality factors are obtained by adjusting the gap spacing between two SSIRs and the tapped position of the feedlines. Their values are: $Q_{e1} = 34.21$ and $k_1 = 0.0421$ for the first band; $Q_{e2} = 11.22$ and $k_2 = 0.128$ for the second band; $Q_{e3} = 22.3$ and $k_3 = 0.06$ for the third band, and $Q_{e4} = 19.39$ and $k_4 = 0.0707$ for the fourth band.

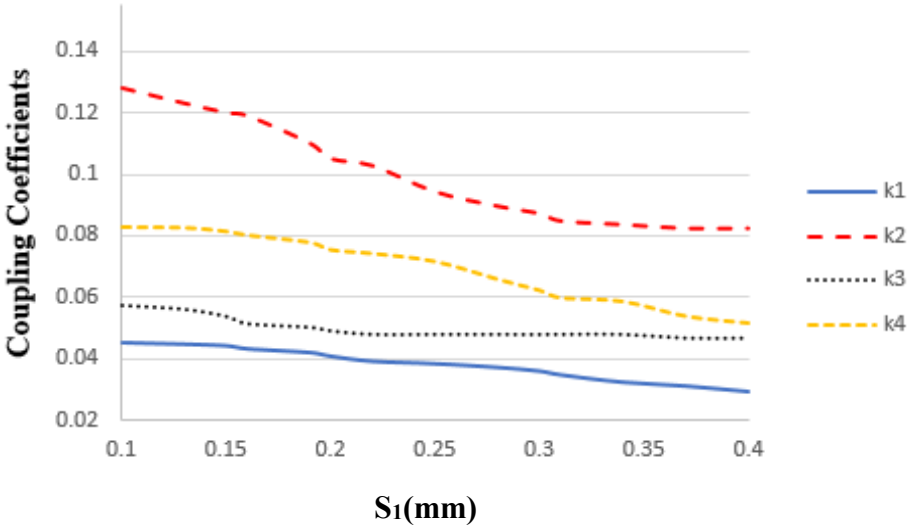
Coupling Coefficients
0.14
0.12
0.1
0.08
0.06
0.04
0.02
0.1
0.15
0.2
0.25
0.3
0.35
0.4
S1(mm)
k1
k2
k3
k4

(a)

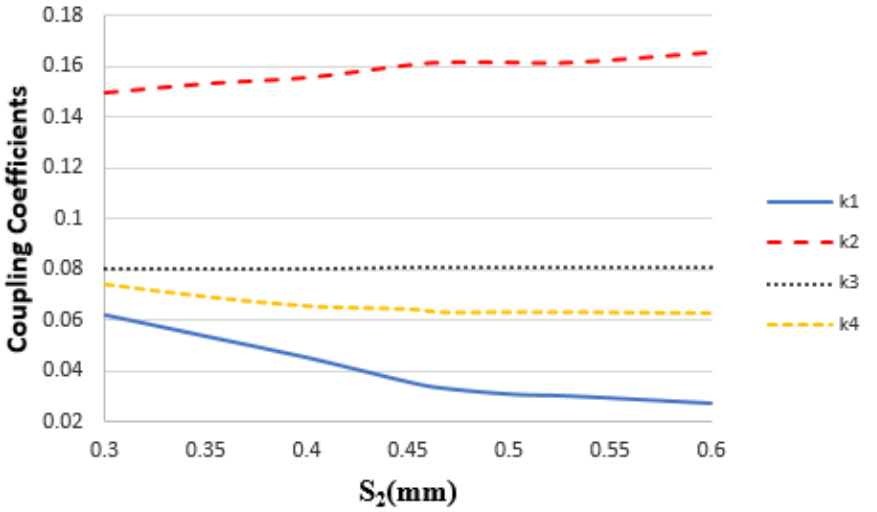
Coupling Coefficients
0.18
0.16
0.14
0.12
0.1
0.08
0.06
0.04
0.02
0.3
0.35
0.4
0.45
0.5
0.55
0.6
S2(mm)
k1
k2
k3
k4

(b)

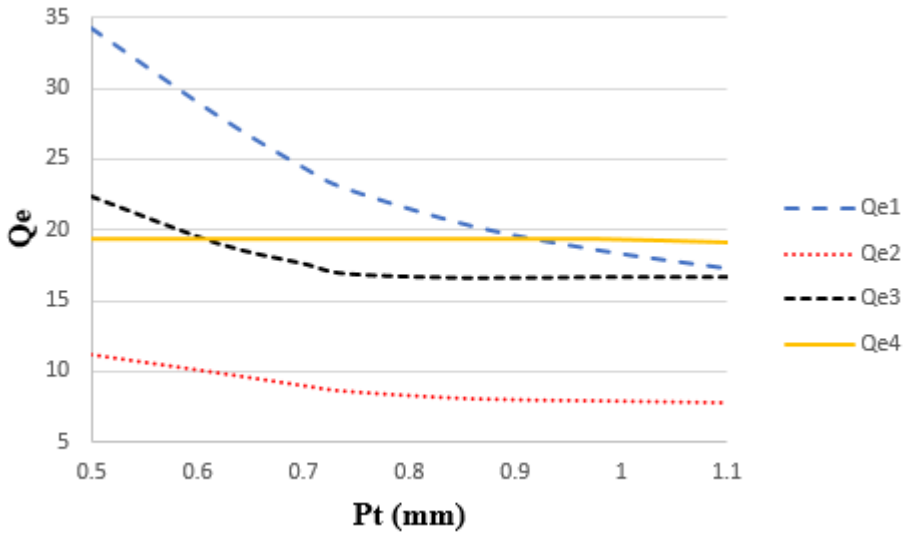

(c)

Figure 3.27 Spacing gap resonator on each layer versus coupling coefficients. (a) Metal layer1 (b) Metal layer 2 (c) The Qe versus taped feed position

Figures 3.27 (a) and (b) show the coupling coefficients with respect to the resonator gap spacings in the first and third layer, respectively. According to Figure 3-27 (a), when S_1 increases, the coupling coefficients associated with the second and fourth passbands are obviously decreased with a slight change in the coupling coefficients associated with the first and third passbands. This is because the resonator gap spacing in the first layer dominates the electric coupling of the second and fourth passbands. It has been further observed from HFSS simulations that the second and fourth coupling coefficients, k_2 and k_4, are strongly affected by the resonator gap spacing in the first layer, while the first coupling coefficient k_1 is significantly affected by the resonator gap spacing in the second layer.

Figure 3.27 (c) shows the Q_e with respect to the position of tape feed (P_t). Q_e decreases as P_t increases. Figure 3-28 compares the magnitudes of S_{11} and S_{21} between simulation and measurement, indicating a good agreement over a frequency range up to 22 GHz. The measured return losses in all passbands are larger than 12 dB. Moreover, the measured insertion losses are less than 2.5, 1.1, 1.5, and 2.2 dB in the first, second, third and fourth passband, respectively.

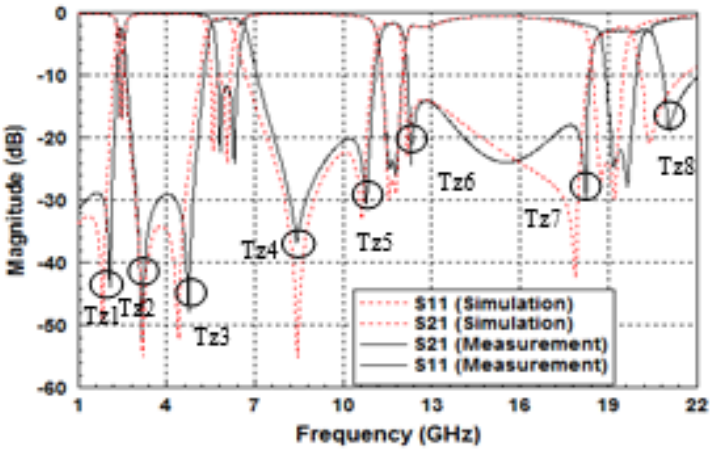

Figure 3.28 Simulated and measured magnitudes of S11 and S21 of the designed quadband BPF.

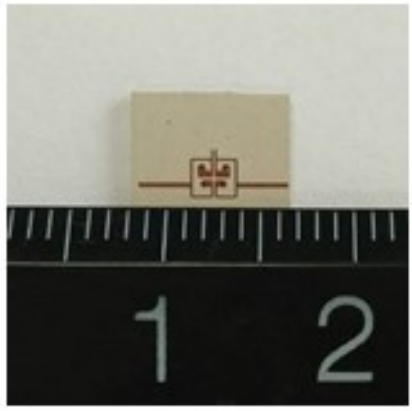

Figure 3.29 Photograph of the fabricated quad-band BPF.

The change in the gap spacing between the two SSIRs affects the electric coupling and can therefore leads to a shift in TZ frequencies. Figure 3.30 shows the change of the TZ frequencies as the gap spacing in the first layer S_1 varies. According to Figure 3-30, when S_1 increases, the fourth and seventh TZs move largely to higher frequencies while the fifth TZ shifts obviously to a lower frequency. Meanwhile, the frequencies of the first and sixth TZs remain almost the same frequency. Moreover, the frequencies of the second, third and eighth TZs slightly shift to higher frequencies. This means that the gap spacing in the first layer affects much on the second and fourth passbands. Figure 3.31 shows how the gap spacing in the second metal layer S_2 influences on the change of TZ frequencies. It reveals that all the TZs except the eighth one shift to higher frequencies as S_2 increases.

Since the gap spacings S_1 and S_2 influence all the TZ frequencies and coupling coefficients, the bandwidth and selectivity of all passbands should be taken into consideration simultaneously in the design procedure. It is commented that the first and third passbands can be well adjusted by changing S_2 while the second and fourth passbands can be well adjusted by changing S_1.

This work also proposes a simple approach for tuning the TZ frequencies. The proposed approach varies the diameter of the annular ring slots for use in isolating the two interconnection via holes from the ground plane. The purpose of doing so is to change the inductance L_{slot} and the capacitance C_{slot} in (Eqn. 3.6) and (Eqn. 3.7) to adjust the TZ frequencies without altering the geometry of the SSIRs. Figure 3-32 shows the change of the TZ frequencies as a function of the diameter of the annular ring slots. As this diameter decreases, the TZs move closer to the passbands, causing a higher rolloff rate in the passband-to-stopband transition. However, this is at a cost of reducing the minimum rejection level in the stopbands since the electric coupling becomes weakened. As this diameter increases, the fourth and seventh TZs move largely to higher frequencies while the others remain almost the same frequency.

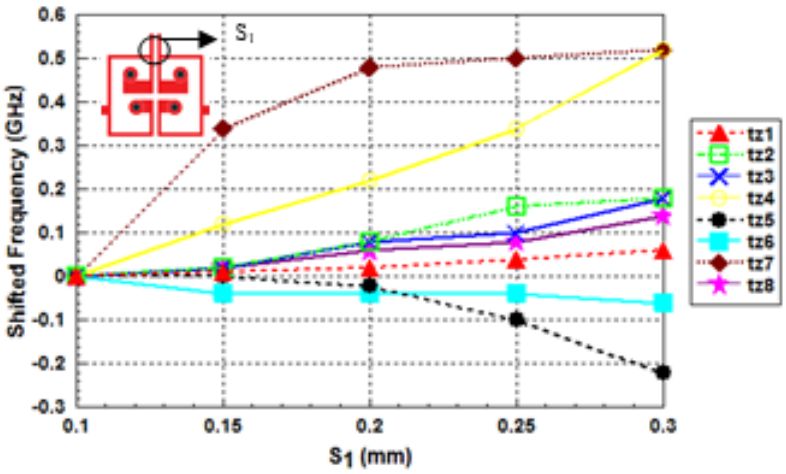

Figure 3.30 TZ frequencies versus the gap width on the first layer.

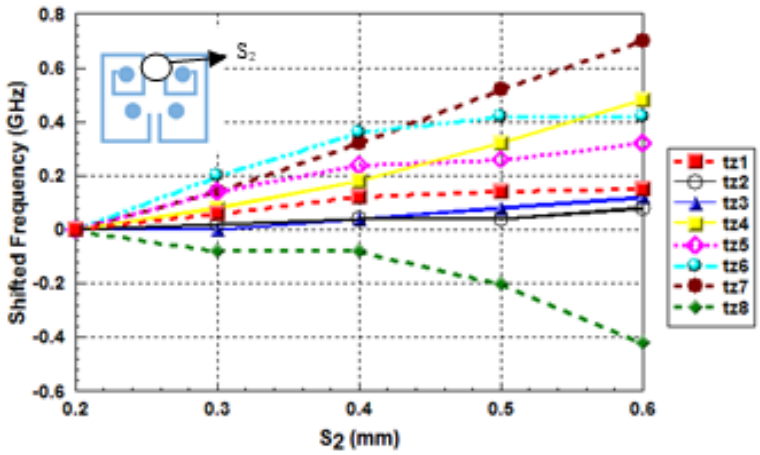

Figure 3.31 TZ frequencies versus the gap width on the second layer.

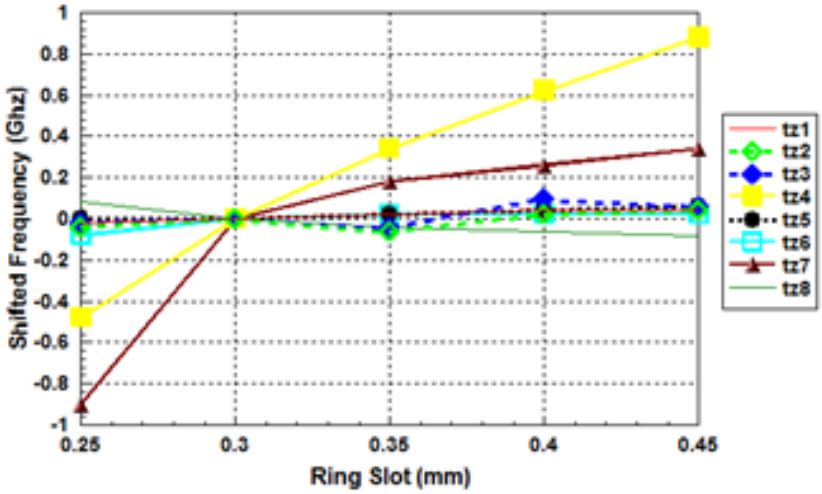

Figure 3.32 TZ frequencies versus the diameter of ring slots.

Table 2 Performance comparison of quad-band BPFs

Reference Number	Substrate parameter	Passband center frequency (GHz)	3-dB FBW (%)	Passband insertion loss (dB)	Size (mm) &(λg)
38	ε_r = 3.38 h = 0.508	2.8/4.2 2.0/3.1	3.6%/4.0% 5.3%/5.7%	2.9/2.3 2.1/2.2	49.6 x 18.2 (0.85 x 0.31)
42	ε_r = 10.8, h = 1.27	1.8/5.8 2.4/5.8	16.2%/9.5% 8.8%/5.4%	0.61/1.5 2.05/2.05	24.33 x 6.85 (0.48 x 0.14)
43	ε_r = 2.2, h = 0.508	2.4/5.2 2.45/5.7	-	<1.5/<1.4 <1.4/<1.4	9.8 x 9.7 (0.12 x 0.12)
16	ε_r = 2.2, h = 0.787	2.4/3.5/5.4/6.8	5.8%/11.2% / 4.4%/5.3%	<2.8	13 x 14.5 (0.15 x 0.172)
Proposed design	ε_r = 10.2, h = 0.568	2.4/5.8/11.6/19	4.1%/12.5% / 6.29%/7%,	2.5/1.1/1.5/ 2.2	2.6 x 2.5 (0.066x0.063)

Table-2 compares the performance between the proposed quad-band BPF and the previous works. It can be seen that the proposed design has lower insertion loss and smaller size because of the use of the multilayer structure.